Synchrotron X-ray micro-tomography investigation of the early hydration of blended cements: A case study on CaCl2-accelerated slag-based blended cements

Mathilde Poirier, Simon Blotevogel, Catherine Noiriel, Anne Bonnin, Judit Kaknics, Margie Olbinado, Laurent Steger, Cédric Patapy, Martin Cyr

Synchrotron X-ray micro-tomography investigation of the early hydration of blended cements: a case study on $CaCl_2$-accelerated slag-based blended cements

Mathilde Poirier[1,2*], Simon Blotevogel[2], Catherine Noiriel[3], Anne Bonnin[4], Judit Kaknics[5], Margie Olbinado[4], Laurent Steger[1], Cédric Patapy[2], Martin Cyr[2]

[*] Corresponding author: mathilde.l.poirier@gmail.com, Tel. (+33)561556711, Fax (+33)561556265

[1] Ecocem Materials, 324061 Block F1, Eastpoint Business Park, Dublin 3, Ireland

[2] Laboratoire Matériaux et Durabilité des Constructions (LMDC), Université Paul Sabatier, INSA/UPS Génie Civil, Université de Toulouse, 135 Avenue de Rangueil 31077 Toulouse Cedex 04, France

[3] Géosciences Environnement Toulouse, Observatoire Midi Pyrénées, Université Paul Sabatier, CNRS, IRD, CNES, Université de Toulouse, 14 avenue Edouard Belin, 31400 Toulouse, France

[4] Paul Scherrer Institute (PSI), TOMCAT beamline, Forschungstrasse 111 5232 Villigen PSI Switzerland

[5] ArcelorMittal Maizieres Research, Voie Romaine, 57283 Maizières-les-Metz, France

Abstract

In situ X-ray Micro-Tomography (XMT) analyses with a pixel size of 0.325 µm were conducted on slag-based blended cements containing 75% of Ground-Granulated Blast-Furnace Slags (GGBS) and 25% of Ordinary Portland Cement (OPC), with or without $CaCl_2$ acceleration. Results show the identification of the main cementitious phases and the need to perform data repeatability tests in order to allow their quantification. Investigation of the early hydration during the first 31 h of hydration by image subtraction showed (i) the dissolution of OPC/GGBS, (ii) the precipitation of hydrates including C-S-H, (iii) the accelerating effect of $CaCl_2$, and (iv) phase-identification based on their specific grey level.

Keywords: *In situ* X-ray Computed Micro-Tomography, low-carbon cement, early hydration, microstructure, repeatability, image subtraction.

This manuscript was published in "Construction and Building Materials" under doi : 10.1016/j.conbuildmat.2022.126412

I. Introduction

Blended cements with high substitution rates of Ordinary Portland Cement (OPC) by Supplementary Cementitious Materials (SCMs) have the potential to significantly lower CO_2 emissions in the construction industry. Typical SCMs include blast-furnace slag, fly ash, silica fume, natural pozzolans, metakaolin and limestone [1–4]. At high substitution rates (>20-30%), the early strength development of blended cements is, however, reduced compared to plain OPC, because most SCMs have slower hydration rates than clinker phases [5,6]. Accelerating admixtures such as calcium chloride ($CaCl_2$) improve the early age reactivity and microstructure development of blended cements [7–10].

Cement hydration is a coupled dissolution/precipitation reaction, where clinker (C_3S, C_2S, C_3A, C_4AF) and SCM phases dissolve in a basic medium to precipitate hydrate minerals such as C-S-H, portlandite (CH), ettringite and AFm in the pore space. Traditional tools to investigate the hydration reaction include Scanning Electron Microscopy (SEM), X-Ray Diffraction (XRD), solid-state Nuclear Magnetic Resonance spectroscopy (NMR), Thermogravimetric analyses (TGA), isothermal calorimetry and mercury intrusion porosimetry (MIP) [11]. These techniques are suitable for observing, identifying and/or quantifying the evolution of the unreacted phases, hydrates and porosity during hydration. However, at early ages of hydration (i.e., during the first 48 h), the use of conventional tools is limited by sample preparation as (i) early age blended cement pastes have not hardened enough to be cut, polished and resined for SEM observation [12], (ii) the physicochemical reactions progress quickly, which requires a hydration stoppage (usually leading to microstructure alterations) [13], and (iii) carbonation, i.e., reaction between hydrated phases and CO_2, is a supplementary source of degradation of the original matrix [11]. In addition, SCM hydration is sometimes difficult to monitor and to discriminate from that of OPC, as dissolution of both SCM and OPC leads to similar hydration products (e.g., C-S-H), and because most SCMs are amorphous alumino-silicates hardly detectable by common lab devices [3]. In theory, an ideal tool to investigate the early hydration of blended cements would involve (i) an *in situ* analysis, and thus no hydration stoppage, (ii) short acquisition times, and (iii) the possibility of differentiating between the SCM and OPC reactions.

Synchrotron X-ray Micro-Tomography (XMT) allows 3D visualization of a given sample using a pixel size of about 1 µm under *in situ* conditions. This technique has been used to study the microstructure, degree of hydration, permeability, fracturing, and damage of various cements at later stages of hydration [12,14–17]. A 3D volume of a sample is reconstructed from thousands of 2D images recorded at various angles [18–21]. The 2D projections, also called radiographs, record the variations in the X-ray linear attenuation coefficients μ, which are dependent on the incident X-ray beam energy, and elemental composition and density of the sample components. In cements, Gastaldi et al., 2012 have reported a μ value of 1.8 cm^{-1} for water, 17.5 cm^{-1} for ettringite, 32.0 cm^{-1} for C-S-H, 44.8 cm^{-1} for portlandite, 55.8 cm^{-1} for C_3A, 63.1 cm^{-1} for C_2S, 65.4 cm^{-1} for C_3S, and 102.6 cm^{-1} for C_4AF, for an

incident beam energy of 14 keV [22]. The relatively close μ values imply that most of the phases have low grey level contrasts on the XMT images and corresponding histograms. Nevertheless, the porosity, hydration products, and anhydrous phases can be differentiated.

Lately, XMT has been used to study the early hydration of various highly reactive cements [12,22–24]. In most studies, the same samples are scanned at fixed time intervals during the first day(s) of hydration, and the resulting XMT images and corresponding grey level histograms are compared to evidence (i) the progressive dissolution of clinker phases, (ii) the precipitation of hydrates, and (iii) the reduction of porosity. For example, Chotard et al., 2003 studied the microstructure development of a calcium aluminate cement between 1 and 24 h of hydration, and showed that the X-ray linear attenuation coefficient varied with the hydration time. Helfen et al., 2005 investigated the formation and development of microcracks and pores in an OPC paste between 8.4 and 16.5 h of hydration. Gastaldi et al., 2012 monitored the precipitation and dissolution of cementitious phases from 1 to 12 h on three cement pastes (OPC, calcium sulfoaluminate cement (CSA) and an OPC/CSA mix), and proposed a new method to determine the specific grey levels of various cementitious products in the histograms. Finally, Parisatto et al., 2015 evaluated the influence of the water/cement ratio on two OPC pastes, from 1.75 to 71 h of hydration. Most of the time, the microstructural changes were evidenced on histograms because of the complexity and heterogeneity of the materials in the XMT images. Image segmentation was performed in order to quantify the amount of cementitious phases on a Representative Elementary Volume (REV), which *a priori* represents the structural and macroscopic properties of the material [12,14,25–28].

From the above-cited literature, XMT appeared ready for common use to monitor early hydration. Therefore, in the present study, XMT was used to investigate more complex and slower reacting materials, i.e. blended cements containing 75% of Ground-Granulated Blast-furnace Slags (GGBS) as SCM and 25% of OPC, with or without $CaCl_2$ addition as an accelerator. The samples were cast into 300 µm capillaries and scanned during the first 31 h of hydration, resulting in XMT images with a pixel size of 0.325 µm. The images were first qualitatively analyzed by morphological and histogram analyses in order to identify the cementitious phases. Then, the REV size was determined in view of phase quantification. Data repeatability tests were carried out in order to evaluate the method error. Early hydration was further investigated by based on histograms and image comparisons of samples scanned at different hydration times. Finally, image subtraction was used to evidence the hydration reactions, such as the dissolution of the anhydrous phases, precipitation of hydrates, as well as their specificities (spatial distributions, specific grey levels in the histograms).

II. Materials & Methods

2.1. Sample preparation

GGBS (produced by ArcelorMittal, and ground/commercialized by Ecocem Materials) and OPC (CEM I 52.5R, Lafarge) were used as raw materials to prepare slag-blended cement pastes composed of 75% GGBS and 25% OPC with a water/binder ratio of 0.4 by mass. Powders were mixed and hand-stirred for 2 min after addition of water. The mixing water was distilled water for the non-accelerated samples, and a 1 wt.% $CaCl_2.2H_2O$ solution (Sigma-Aldrich) for the accelerated samples [29]. After homogenization, the pastes were cast in 300 µm borosilicate capillaries by applying slight underpressure (WJM-Glas, Müller GmbH) 6 hours or 24 hours prior to the measurements. The capillaries were then sealed and stuck into sample holders.

Six samples were prepared to represent the desired compositions and hydration times (Table 1). Two of them were hydrated for 6 h or 24 h without $CaCl_2$ activation (S75_6h and S75_24h) and two replicates (R) were prepared in order to estimate the method error (S75_6h_R and S75_24h_R). Two samples were accelerated with 1 wt.% of $CaCl_2$ and hydrated for 6 h or 24 h (S75_$CaCl_2$_6h and S75_$CaCl_2$_24h). The 6 capillaries were rescanned about six hours after the initial scan in order to monitor the early hydration. The suffix "rescan+xh" was added to their name, where xh refers to time elapsed after the initial scan.

Table 1: List of samples

Name of samples	Hydration time of initial scan	$CaCl_2$ activation	Name of rescans	Hydration time of rescan
S75_6h	6h	No	S75_6h_rescan+5h30	11h30
S75_24h	24h	No	S75_24h_rescan+7h15	31h15
S75_6h_R	6h	No	S75_6h_R_rescan+5h05	11h05
S75_24h_R	24h	No	S75_24h_R_rescan+7h15	31h15
S75_$CaCl_2$_6h	6h	Yes	S75_$CaCl_2$_6h_rescan+5h20	11h20
S75_$CaCl_2$_24h	24h	Yes	S75_$CaCl_2$_24h_rescan+6h50	30h50

2.2. X-ray micro-tomography imaging

XMT analyses were carried out at the Swiss Light Source (SLS) of the Paul Scherrer Institut, Switzerland, on the TOMCAT beamline. A beam energy of 21 keV was chosen for imaging all samples, providing a high photon flux that permits fast scans. Transmitted X-ray photons were converted into visible light using a 20 µm LuAG:Ce Scintillator, and 1501 projections were taken over an angular range of 180° with an exposure time of 180 ms each. This setting led to a scanning time of about 15 min per sample, and enabled quick mapping of the hydration reaction. Diffraction-limited microscope optics and

a PCO.Edge 5.5 camera were used to magnify (× 20) and capture the radiographs. Images were corrected for the noise of the camera (dark field subtraction) and for inhomogeneities of the beam (divided by flat field). Phase retrieval [30] was also applied prior to the tomography reconstruction [31] using a Paganin algorithm. A distance of 5 mm and a delta/beta ratio of 100 were chosen for the reconstruction. Each reconstruction was of 2560 × 2560 × 2160 voxels with isotropic size of 0.325 µm. This image resolution is about 5 and 1.5 times higher than that reported in other XMT studies on slag-blended cements [16,32–36] and OPC pastes [12,14,25,28], respectively.

2.3. XMT data processing

The reconstructed volumes were processed using the Avizo® software on a Dell Precision T3600 workstation (64 GB RAM, 6 GB Nvidia graphics card). The 16-bit data sets were first normalized and reduced to 8-bit data sets in order to reduce the amount of data to be processed. During normalization, the grey level ranges were calibrated between initial scans and rescanned images using a linear interpolation procedure, assigning fixed values to the exterior air signal and the GGBS signal maximum peaks. After 8-bit conversion, the calibrated greyscale of the images ranged from 0 to 255. To allow for further image comparison, each image pair was then registered in the same (x,y,z) coordinate system using a rigid-body transformation based on mutual information optimizer. Finally, image subtraction was performed twofold, either by subtracting the initial scan to the rescan image or vice-versa, thus offering the possibility to distinguish the solid phases that disappeared from the ones that formed during the hydration process.

Visualization and quantification of the OPC/GGBS dissolution, removal of transitional dense phase in the pore space, and precipitation of portlandite and hydrates* was performed on subvolumes of 200 × 200 × 600 µm after image subtraction and a simple thresholding method (see section 3.3.1 for details). Note that hydrates* refers to all hydrate phases except portlandite, e.g. C-S-H, AFm and ettringite for slag based blended cements. The upper and lower thresholding values were chosen manually in order to extract the phase(s) of interest identified based on their morphology, and minimize the contribution of the other phases due to overlapping grey levels.

III. Results and Discussion

3.1. Preliminary study of XMT images

3.1.1. Identification of phases

Figure 1 shows a slice of slag-blended cement with the corresponding histogram extracted from the subvolume of 200 × 200 × 600 µm. The cementitious phases were identified by morphological analysis and comparison of histograms with the literature [14,22,37]. Seven main phases were identified:

- porosity in dark grey level (air bubbles, water filled pore network),

- hydrates* in fairly dark grey level (small interconnected particles in the pore network),
- portlandite in intermediate grey level (zones of irregular shape with a grey level in the GGBS range),
- GGBS in light grey (angular grains of various particle sizes),
- OPC in very light grey level (rounded grains),
- and metallic iron particles in white (local bright spots).

In addition, a transitional dense phase was systematically observed in the pore space, except for S75_24h (see further, the blue arrows in Figure 3.a). This phase exhibited an irregular shape and was distributed very heterogeneously in the samples. It had an intensity in the darker range of the grey levels of hydrates*, and appeared as a grey background in the pore network. Only a high magnification allowed it to be distinguished from hydrates*. Analysis of the later samples (Figure 3.b) showed that the phase disappeared in all samples after the first few hours of hydration, while the hydrates remained in place. After 31 h of hydration, the transitional dense phase was no longer present in the rescanned samples. Therefore, it is unlikely that this phase consisted of solid hydrates. According to its morphology, behavior, and relatively high absorption coefficient, the transitional dense phase was attributed to a mobile pore water enriched in ions or nuclei. As far as we know, no previous study conducted on OPC or slag-based cements has reported this transitional dense phase. It may form according to the following processes: first of all, the high proportion of GGBS (75 wt.%) and its slow dissolution rates compared to clinker phases allows Ca and Si ions to diffuse into the pore space, so they do not necessarily precipitate around slag grains [38]. This makes stronger oversaturation and nucleation in solution possible. Secondly, the resolution here was 5 times higher than that reported in other slag-based cement studies [16,32–36,39]. Therefore, other authors may not have observed it, or may have confused it with hydrates*.

The histograms derived from image analysis of the subvolumes were composed of four major peaks centered around grey levels of 35 for porosity (peak A), 70 for hydrates and transitional dense phase (peak B), 120 for GGBS and portlandite (peak C), and 150 for OPC (peak D). The respective phases overlap strongly in the histograms. For example, GGBS and CH are strongly convoluted and no thresholding method could differentiate between the two phases. The peak areas in the histogram are proportional to the amounts of corresponding phases in the samples.

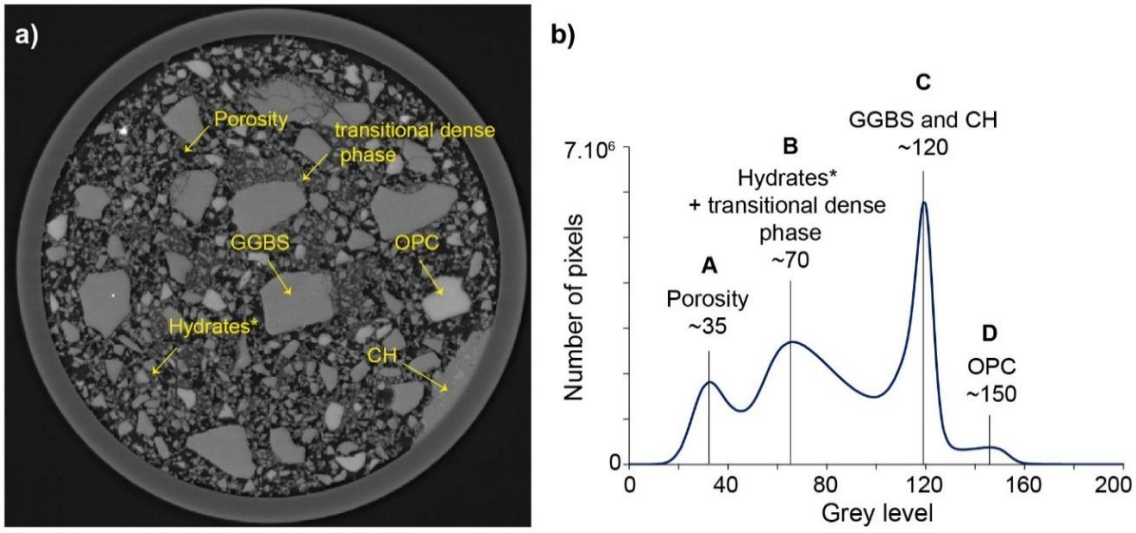

Figure 1: Identification of the cementitious phases in the XMT image of S75_$CaCl_2$_6h and in the corresponding histogram.

3.1.2. Determination of the Representative Elementary Volume (REV)

XMT often produces large datasets. In order to reduce the amount of data to be processed and to avoid edge effects, a smaller volume, called Representative Elementary Volume (REV) can be extracted. This volume corresponds to the smallest volume representing the structural and macroscopic properties of a given material. In practice, several techniques allow the REV size to be determined [40,41]. In this study, the methodology of Wan et al., 2014 was applied. This method measures the porosity in cubic volumes of increasing size, starting from a random point in the capillary. The measurement is performed multiple times in order to evaluate the smallest volume at which porosity converges to a constant value. This volume defines the REV.

Figure 2.a. shows an example of the REV determination on S75_6h_rescan+5h30. The porosity was measured by thresholding the fluid (porosity) from the solid phase in the histogram (grey level value = 50). The cube edge size was increased progressively from 5 µm to 220 µm from a random point. The procedure was repeated 5 times in different areas of the sample. The porosity converged from an edge size of 100 µm onwards, and stabilized around 200 µm. This value corresponds to the REV size, which is equal to a cubic volume of about 8.10^6 μm^3 and a mean porosity of 14% (Figure 2.c, red volume). Note that the REV size is similar to that calculated in previous studies [14,36]. However, it is worth mentioning that REV could not be determined in the initial scans of this sample (Figure 2.b) due to the presence of the transitional dense phase in the pore space, which led to an underestimation of the porosity since its grey level fell into the range of hydrates* (while it should account for porosity). In the initial scan, no convergence was found for volumes with up to 220 µm edge length; the calculated mean porosities were 3 to 6 times lower (2.5 to 5.0 %) than in the rescan (14%). Even by further increasing the subvolume size to 200 × 200 × 600 µm a porosity of 3.3 % was calculated, taking almost the whole

capillary into account but still avoiding edge effects (Figure 2.c, blue volume). We decided to extract the histograms on subvolumes of 200 × 200 × 600 µm to compare the initial scan and the rescanned samples in order to avoid artifacts due to the heterogeneous distribution of the transitional dense phase.

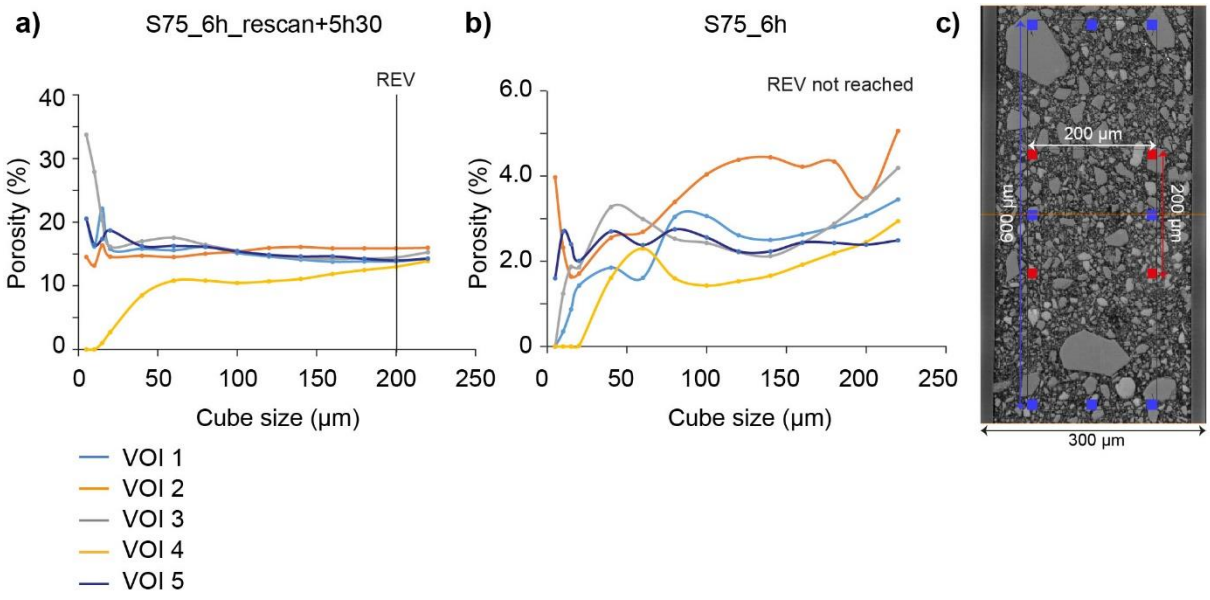

Figure 2: a) Determination of the REV size on S75_6h_rescan+5h30, according to the methodology of Wan et al., 2014 (VOI: Volume Of Interest). b) Attempt at REV determination on S75_6h, which contained a large amount of transitional dense phase in the pore space. c) Representation of the two subvolumes of 200 × 200 × 600 µm (blue) and 200 × 200 × 200 µm (red: REV).

3.1.3. Evaluation of experiment repeatability

Repeatability refers to the closeness of the agreement between several tests carried out under similar conditions [42]. In this study, two samples (S75_6h and S75_24h) were replicated (S75_6h_R and S75_24h_R) in order to check the repeatability of the experiment, and because data repeatability is rarely reported in the literature. Figure 3, lines 1 to 4, shows the initial scan and rescanned slices of these samples, and their corresponding histograms. Differences in peak height of about 20% for peaks B, C, and D, and of about 80% for peak A were observed between S75_6h and S75_6h_R. In S75_24h, the peaks A and B were not distinguishable, while there were two distinct peaks in S75_24h_R. In addition, peak C was around 15% higher in S75_24h than in S75_24h_R, but thinner. Surprisingly, this means that two samples prepared in two different capillaries showed substantial differences in the fluid and mineral phase distribution despite the fact that REV was reached. This implies that comparison of histograms and absolute quantifications were limited to variations greater than the measurement error.

Two reasons may explain the lack of data repeatability. First of all, the heterogeneous distribution and variable amount of the transitional dense phase in the pore space may have induced variations in the intensity of peak B. However, this explanation cannot account for the variations of peaks C and D, as

these peaks are not correlated to the presence of the transitional dense phase. The second reason may arise from the small size of the capillaries (300 µm), which may have lowered the paste homogenization and prevented the sample preparation to be repeatable. However, glass capillaries of few hundred micrometers are regularly used in the literature, resulting in the use of regions of interest smaller or similar to the subvolume size (200 × 200 × 600 µm) used in this study for phase quantifications [12,14,22,25]. Therefore, our experimental methodology can be considered in line with that reported in the literature. Our results should encourage future studies to control their data repeatability in order to allow for quantitative comparisons. In our case, only qualitative analyses were performed.

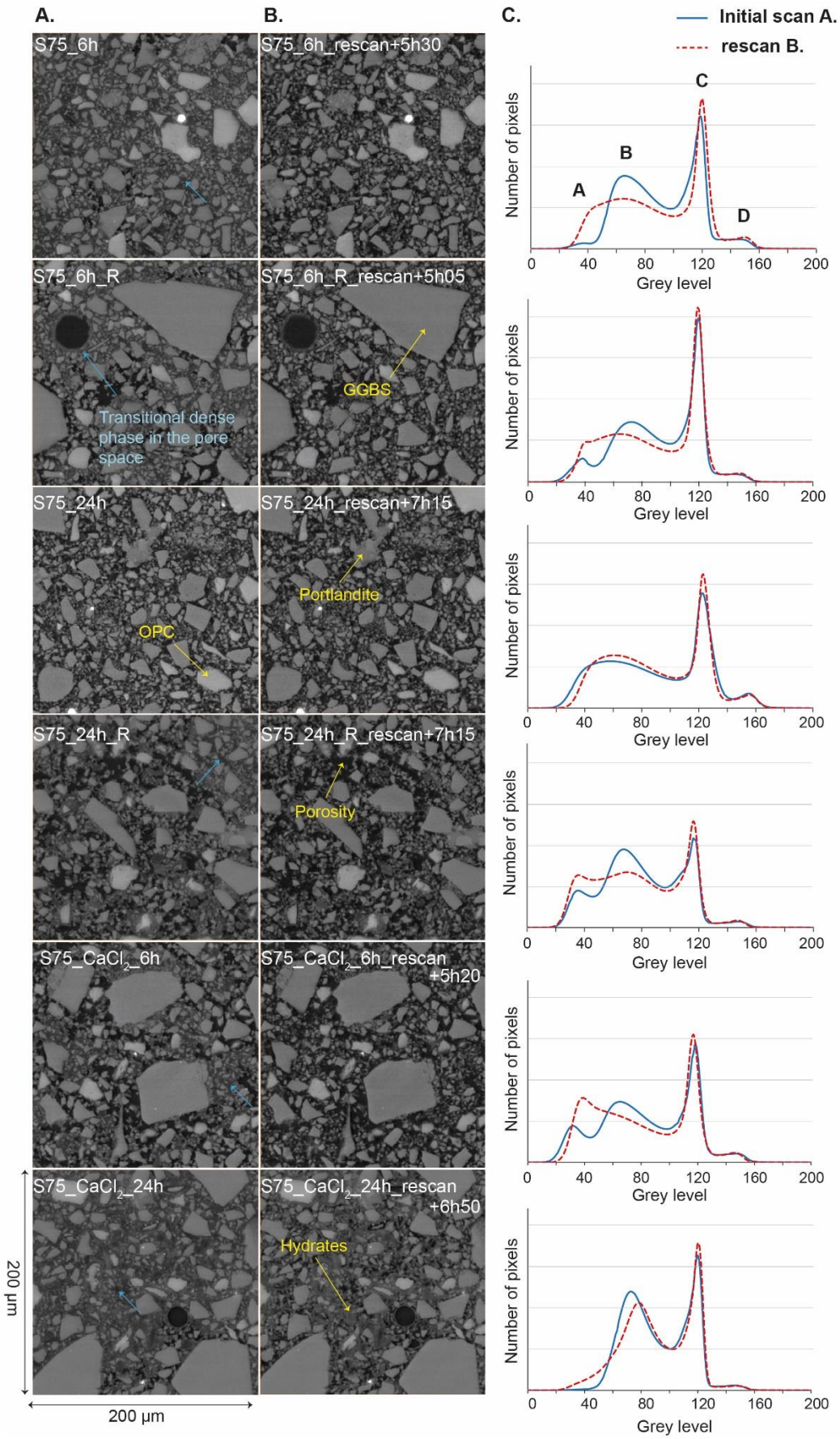
A.
B.
C.
Initial scan A.
rescan B.
S75_6h
S75_6h_rescan+5h30
S75_6h_R
S75_6h_R_rescan+5h05
Transitional dense phase in the pore space
GGBS
S75_24h
S75_24h_rescan+7h15
OPC
Portlandite
S75_24h_R
S75_24h_R_rescan+7h15
Porosity
S75_CaCl2_6h
S75_CaCl2_6h_rescan +5h20
S75_CaCl2_24h
S75_CaCl2_24h_rescan +6h50
Hydrates
200 µm
200 µm
A
B
C
D
Number of pixels
Grey level
0
40
80
120
160
200

242

Figure 3: Influence of the hydration time on the XMT images and histograms: a) Initial scan images, b) rescan images, and c) corresponding histograms taken from subvolumes of 200 × 200 × 600 µm. Note that the replicates S75_6h_R and S75_24h_R do not show the same histogram shapes than the original samples S75_6h and S75_24h, respectively.

3.2 Investigation of the early hydration of blended cements from histograms and image comparison

Early hydration of blended cements was investigated by histogram and image comparison of samples scanned at different hydration ages during the first 31 h of hydration. Since no data repeatability was obtained, no phase quantification was attempted.

Rescans in time and space are useful to monitor the evolution of a single sample during hydration. Indeed, under this configuration, changes in the histogram peak area and shape result from the evolution of sample mineralogy/chemistry, and not from variations induced by inter-sample variability. Figure 3 compares the XMT images of the initial samples (column a), rescanned samples (column b), and corresponding histograms (column c). The first two lines compare the non-accelerated replicates after 6 h and 11 h of hydration, the two following lines compare the non-accelerated replicates after 24 h and 31 h of hydration, and the last two lines the $CaCl_2$-accelerated samples after 6 h and 11 h, and 24 h and 31 h of hydration. The initial scans and rescanned images of each sample show little evolution in the grey level distribution and therefore give little information on the hydration reactions. Only the disappearance of the transitional dense phase in the pore space can be identified (blue arrows). Since the transitional dense phase has a grey level in the range of hydrates* (but, theoretically, should account for porosity), its removal decreases the intensity of peak B, and increases the intensity of peak A in the histograms, leading to the apparent contradiction that older samples contain less hydrates. Information about the precipitation of hydrates* was therefore lost.

Following the dissolution of GGBS/OPC was also difficult, as the XMT images did not show any major changes in particle size during hydration, and no evidence of GGBS/OPC dissolution was observable on the histograms: the intensity of peak C increased during hydration but sharpened, leading to similar peak area, and the intensity of peak D did not show significant variations on either the accelerated or non-accelerated samples. Therefore, image and histogram comparison of rescanned samples did not allow the early hydration to be monitored due to the complex phase assemblage and slow hydration rates of the materials.

3.3. Image subtraction: an alternative method to reveal (blended) cement hydration

3.3.1. Principle of image subtraction

XMT image subtraction reveals small differences in pairs of nearly identical images [43–46]. In this study, the method was applied to early hydration of un-accelerated and $CaCl_2$-accelerated blended

cements. In image subtraction, the initial image of a rescanned sample is subtracted from the final image, or vice-versa. The pixel grey level of the subtraction image "A-B" or "B-A" corresponds to the absolute difference of pixel grey levels between the two images. Negative values are set to 0. In theory, the subtraction image of two strictly identical images should be black, but in the case of cements, the hydration reactions lead to some differences. The A-B images show the dissolution of initially present phases whereas B-A show the newly precipitated phases.

Figure 4 shows an example of subtraction performed on S75_24h_$CaCl_2$ and on its rescan 6 h 50 later (image B). The image of the subtraction "A-B" (Figure 4.c) reveals the dissolution zones of OPC and GGBS, as the difference of pixel grey levels between OPC/GGBS between the initial scans (~150 and 120 respectively), and the resulting porosity (~35) or hydrates (~70) after dissolution or re-precipitation was positive. Note that a green color scale was used to enhance the visibility of the changes in the images. The removal of the transitional dense phase in the pore space was also made visible by this operation, as the difference of pixel grey levels between the transitional dense phase (~70) in the initial scans, and porosity (~35) after its removal was positive. All other chemical transformations leading to null or negative values were set to 0, and appear in black. On the other hand, the B-A subtraction (Figure 4.d.) highlights the precipitation zones of hydrates, as the difference of pixel grey levels between portlandite/hydrates* in the rescans (~120 and ~70 respectively), and the initial pore space (~35) remained positive. A gold color scale was set in the present case. At the end, the superposition of the two subtraction images with the original XMT image reveals a dissolution rim around the OPC grain "1", as well as the precipitation of hydrates* in its vicinity (Figure 4.e). Further information will be extracted in sections 3.3.2 and 3.3.3 by comparing the subtraction images of the un-accelerated and $CaCl_2$-accelerated systems, at various hydration ages.

Segmentation based on simple thresholding was then employed to extract one or more phases from the subtraction images. The thresholding range was set by fitting only the pixel areas of the phase(s) of interest, based on the morphological attribution of section 3.1.1. Either the transitional dense phase in the pore space, GGBS/OPC, or portlandite, and/or other hydrates* could be separated from the other phases in the subtraction image, depending on the thresholding range used. The quality of the extraction depends on the separation of grey levels, since a large overlap would prevent the appropriate thresholding of the phase of interest: if the thresholding range is too large, the phase of interest will be polluted by other phases and, if it is too small, a part of the phase of interest will not be represented. Therefore, a compromise had to be found. In Figure 4.f., only the dissolution of OPC and GGBS was extracted, and the signal of the transitional dense phase was removed. Since the grey levels of OPC edges (~130) and GGBS (~120) overlapped strongly in the histograms, the two phases could not be separated from each other.

After thresholding, a binary image was obtained, and its multiplication with the initial XMT image allowed to represent the selected phase(s) in its original grey scale levels (Figure 4.g). Subsequently, the grey scale histogram of the selected phase(s) was extracted. Finally, the extracted phases were represented in 3D (Figure 4.h). In this study, no quantification was performed due to the non-repeatability of the experiments and the poor quality of the phase extraction (the signal was systematically polluted by other contributions regardless of the phase extracted). However, this step is theoretically possible, and the amount of extracted phase(s) would correspond to the integral of the peak of interest in the histogram of Figure 4.g.

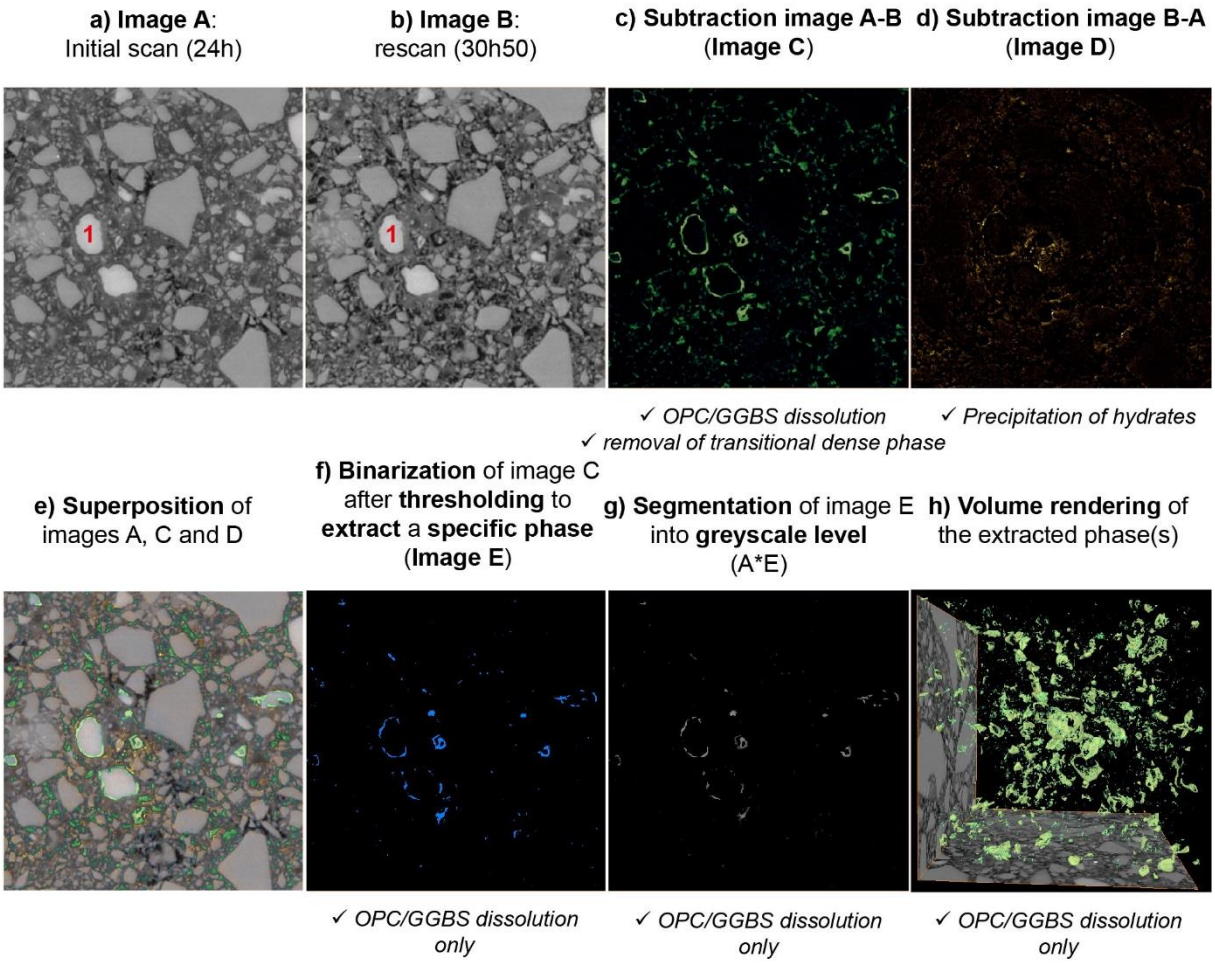

Figure 4: Principle of image subtraction performed on S75_24h_$CaCl_2$ and on its rescan 6 h 50 later.

3.3.2. "A-B" Image subtraction: GGBS/OPC dissolution, removal of transitional dense phase in the pore space

Figure 5 represents the A-B subtraction images of the non-accelerated and $CaCl_2$-accelerated samples, in the hydration ranges of about 6h/11h and 24h/31h. Column 1 shows the extracted phases overlaid on the original XMT images, column 2 the image subtraction only, and column 3 the volume

rendering of the extracted phases (OPC and/or GGBS dissolution, without transitional dense phase in the pore space).

Between 6 h and 11 h of hydration, the subtraction images show mainly removal of the transitional dense phase in the pore space. In the non-accelerated sample (S75_6h/11h), some small GGBS grains also dissolved. Their dissolution appears as a multitude of small bright spots with a size of about 1 – 4 µm in the subtraction image (white arrows in Figure 5). Some bigger GGBS grains (~10 µm) dissolved more locally, as can be seen in the 3D volume. In presence of $CaCl_2$ (S75_$CaCl_2$_6h/11h), less GGBS dissolution was observed, but dissolution rims around the OPC grains were visible (orange arrows in Figure 5). This appears to be in contradiction with a former report on an accelerated slag reaction in presence of $CaCl_2$ [29]. In that study, the contribution of slag to heat release in isothermal calorimetry appeared after 10 hours of hydration in presence of $CaCl_2$, i.e. earlier than the 15 hours of hydration in absence of $CaCl_2$. This corresponds to the appearance of AFm phases in XRD. In our study, it is thus possible that, in the accelerated sample, the initial dissolution of GGBS had already taken place during the first 6 hours of hydration (i.e., before the initial scan), so that this initial dissolution was only visible on the non-accelerated sample.

Between 24 h and 31 h of hydration, no GGBS dissolution was observed in either the non-accelerated or the $CaCl_2$-accelerated samples. This supports the idea that the initial GGBS dissolution had already taken place in the accelerated sample, as no dissolution was observed afterwards (until 31 h of hydration). In absence of $CaCl_2$, only little OPC dissolution was observed in the subtraction images and volume rendering. In presence of $CaCl_2$, the OPC dissolution was stronger and affected almost all OPC grains. The comparison of the two volume renderings showed a clear accelerating effect of $CaCl_2$ on the dissolution of OPC. This is consistent with the fact that $CaCl_2$ accelerates the dissolution of OPC at early ages [29,47–49].

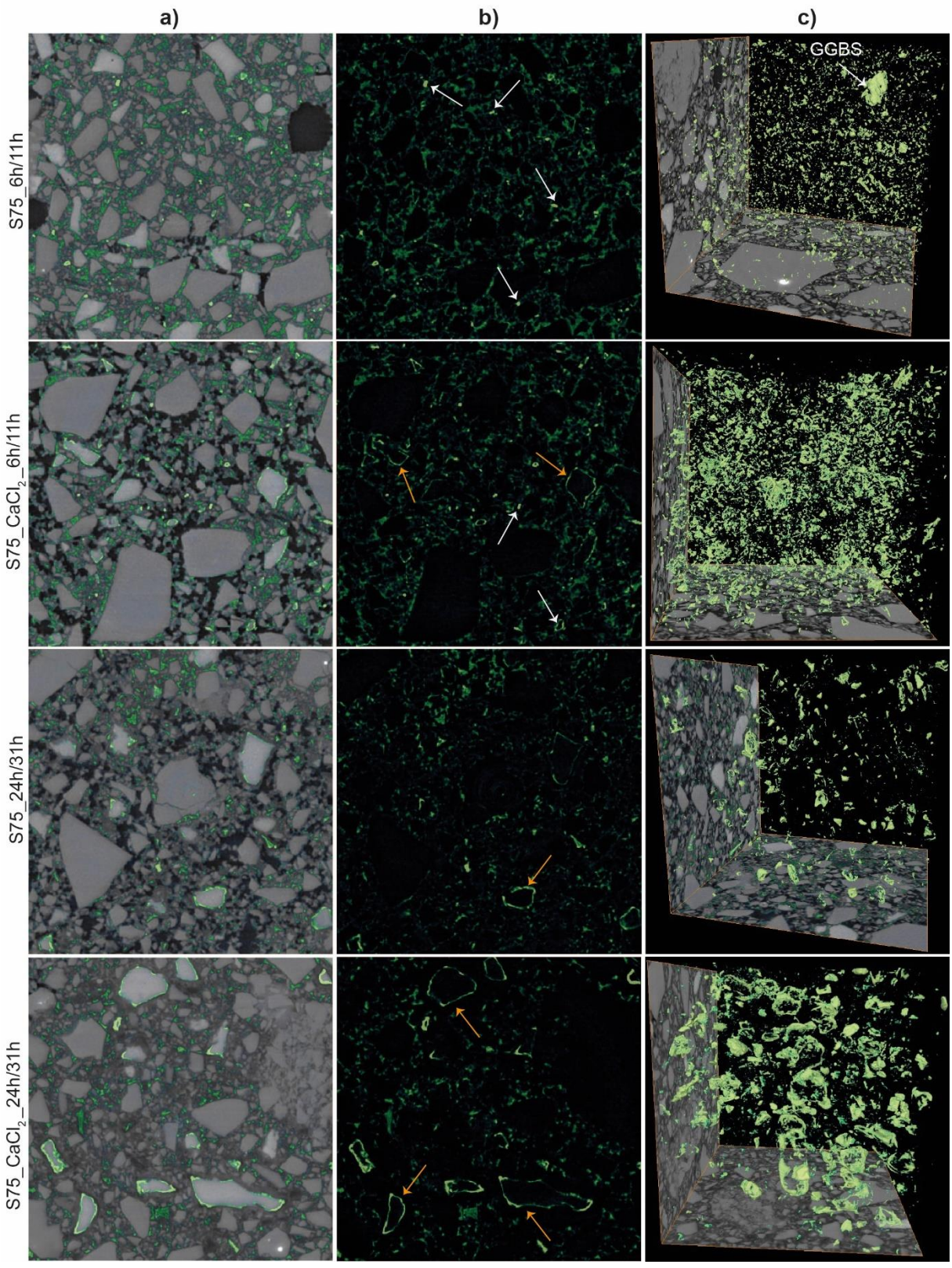

Figure 5: "A-B" image subtractions: a) extracted phases superposed on the original XMT images, b) subtraction images only (OPC/GGBS dissolution, with transitional dense phase in the pore space), and c) volume rendering of the extracted phases (OPC/GGBS dissolution, without transitional dense phase

in the pore space). The arrows were added to highlight dissolution of GGBS (white) and OPC (orange) grains.

3.3.3. "B-A" Image subtraction: precipitation of hydrates

Figure 6 shows the B-A image subtractions of the non-accelerated and $CaCl_2$-accelerated samples. This operation enables visualization of the precipitation of portlandite and/or other hydrates in blended cements.

Between 6 h and 11 h, only the formation of portlandite is visible in the non-accelerated sample. Numerous CH rims appear in both the subtraction image and the volume rendering of Figure 6 (white arrows). The light orange areas may correspond to the precipitation of other hydrates in the pore network, or slight variations in X-ray beam intensity during image acquisition, as some areas fall into the zone of GGBS grains (no precipitation is expected inside GGBS grains). In presence of $CaCl_2$ (S75_$CaCl_2$_6h/11h), less portlandite formation was observed but more other hydrates* precipitated into the pore space (Figure 6, yellow arrows). This is especially visible in the zoom presented in Figure 7. The light orange areas fall almost exclusively within the pore space, which is consistent with faster pore space filling by hydrates* in presence of $CaCl_2$ as previously reported [47–49]. The higher presence of portlandite in S75_6h/11h also agrees with the works of Steger, 2019 [50], who showed more portlandite precipitation at early ages in the non-accelerated slag cements at a similar time scale, by *in-situ* XRD.

Between 24 h and 31 h, precipitation of portlandite almost stopped in both the accelerated and non-accelerated samples. However, in the $CaCl_2$-accelerated paste, an increased formation of other hydrates* was observed around the OPC grains. According to the morphology and localization of the phases, they probably correspond to inner product C-S-H, as they fill the volume of dissolved OPC grains (Figure 6, green arrows and volume rendering). In the non-accelerated sample, no hydrate development was observed, except for very small amounts of portlandite.

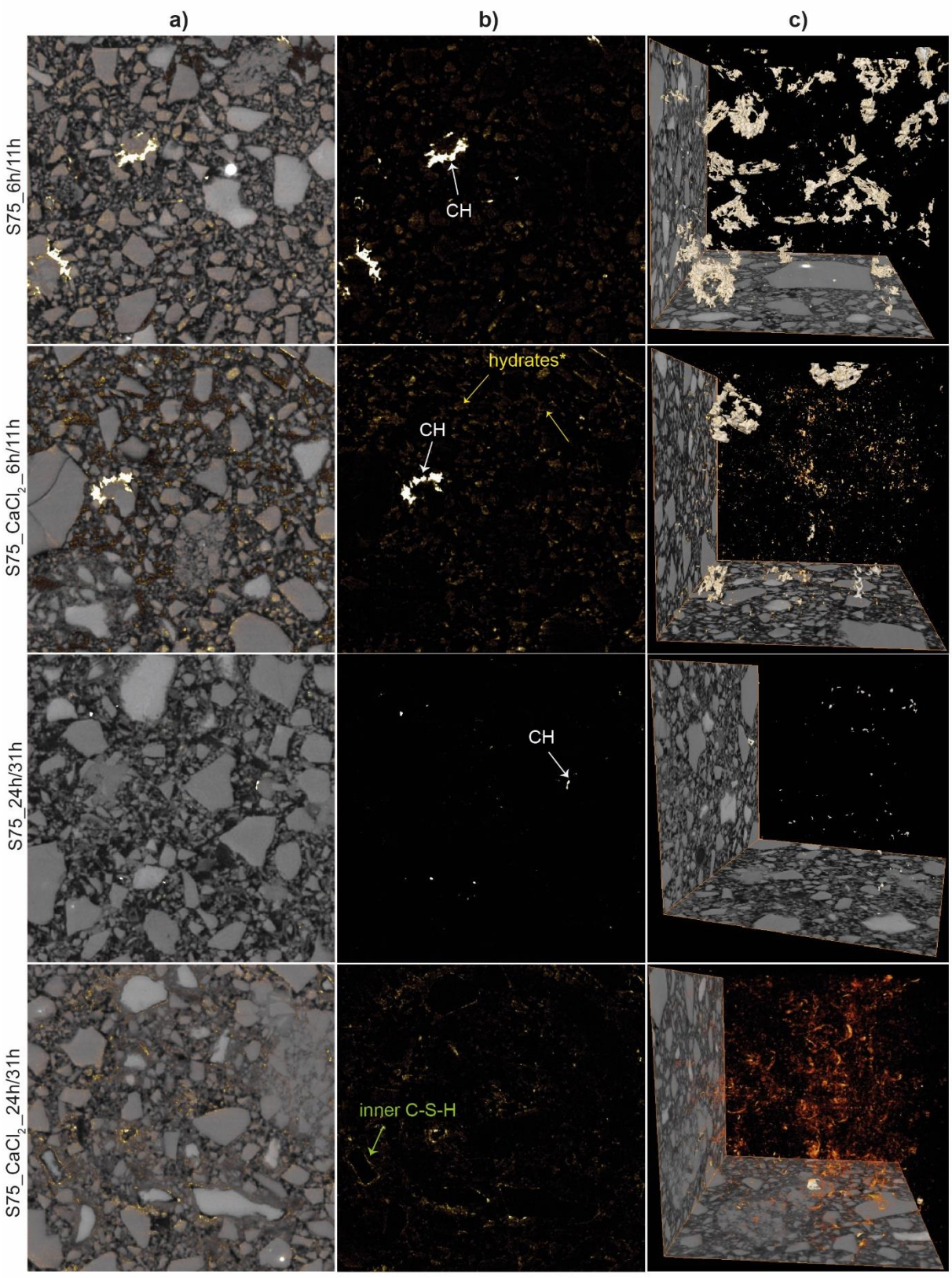

376

377 **Figure 6**: "B-A" image subtractions: a) extracted phases superposed on the original XMT images, b)
378 subtraction images only (CH and/or hydrates* and/or noise), and c) volume rendering of the extracted
379 phases (CH and/or C-S-H).

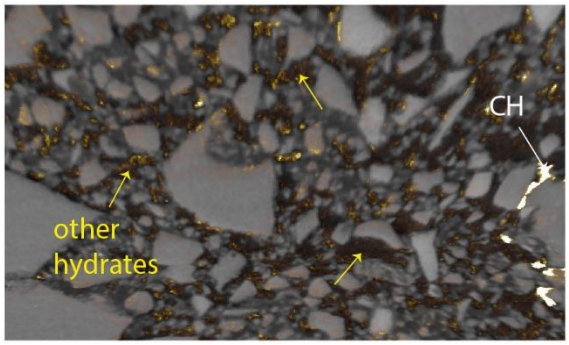

Figure 7: Zoom on the precipitation of hydrates* in the porosity of S75_$CaCl_2$_6h/11h.

3.3.4. Determination of the specific grey levels of the extracted phases by image subtraction

Extraction of the grey level distribution from the histograms after phase segmentation (i.e. Figure 4.g) gave the specific grey levels of the transitional dense phases, i.e., OPC, GGBS, portlandite, and inner C-S-H (Figure 8). The extraction was performed by selecting a specific grey level range of the original images in the subtraction images, which fitted the phase of interest identified base on morphology and comparison with the same spot on the initial scans (see section 3.1.1 and 3.3.1 for details).

The results showed a mean grey level of about ~60 for the transitional dense phase, ~80 for the inner product C-S-H, ~90 for GGBS, ~110 for portlandite and ~120 for OPC. The grey levels overlapped strongly, spanning ± 20 to ± 40 grey level units. Note that the dissolved OPC showed slightly lower grey level (~120) than the average value observed in Figure 1 (~150), probably because of the preferential dissolution of grain edges (Figure 8.b). Edge effects probably associated to partial volume effects / phase contrast decreased the mean grey level of the dissolved OPC compared to the center of the grains. Similarly, in samples where only GGBS was dissolved, the mean grey level of dissolved GGBS is slightly lower (~90) than the average value (~120) determined in section 3.1.1. In systems where OPC and GGBS dissolve, the grey level of the dissolved phases is in between the values for dissolved GGBS (~90) and OPC (~120). Note that in S75_24h/31h, the signal of OPC is very low due to the difficulty of extracting the OPC phase.

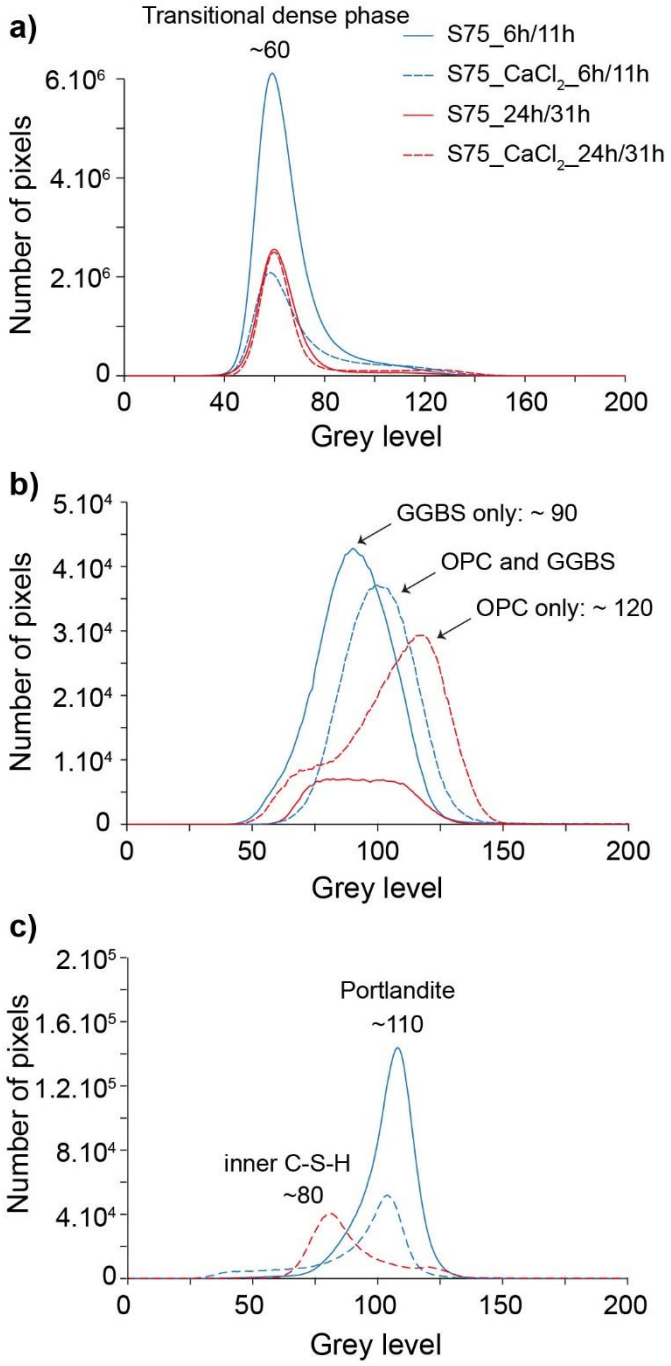

401

402 **Figure 8**: Extraction of the specific grey levels of a) the transitional dense phase in the pore
403 space, b) GGBS and/or OPC, and c) portlandite/inner C-S-H, by combining simple thresholding in the
404 subtraction images with the original image, from (cf. Figures 6 and 7). The number of pixels is not
405 correlated with the amount of a given phase in the samples here, due to the non-repeatability and grey
406 level overlapping.

V. Conclusions

In this study, XMT was used to highlight the early hydration of both $CaCl_2$-accelerated and non-accelerated slag-based blended cements with a pixel size of 0.325 µm. Seven cementitious phases were identified in the XMT images and histograms: porosity, OPC, GGBS, portlandite, other hydrates, metallic iron particles and a transitional dense phase in the pore space with a grey level similar to that of the hydrates. For the first time, data repeatability tests were reported for cement pastes cast into glass capillaries of 300 µm. Surprisingly, different capillaries filled with the same paste do not give repeatable results, despite the fact that the REV size was reached, and that sample preparation was similar to what is frequently presented in the literature. This result should encourage future studies to control the data repeatability before conducting quantitative analyses. The early hydration of samples scanned at different hydration times was then qualitatively investigated during the first 31 h of hydration by histogram and image comparisons. These methods gave only limited information on the hydration reaction, due to the complex phase assemblages and slow hydration rates of the materials. Therefore, image subtraction of the same samples was used as an alternative method in order to evidence small differences in the fluid and solid phases. This method allowed to show (i) the dissolution of OPC and GGBS, (ii) the precipitation of portlandite and inner C-S-H, (iii) the accelerating effect of $CaCl_2$, (iv) the distribution of dissolved/precipitated phases in 3D, and (v) the specific grey levels of the different phases. More specifically, $CaCl_2$ was shown to accelerate the dissolution of OPC and increase the precipitation of hydrates between 6 h and 11 h of hydration. The effect was even stronger between 24-31 h of hydration, with numerous dissolution rims around OPC grains and C-S-H clusters in the pore space. In absence of $CaCl_2$, the dissolution/precipitation reactions were slower and were visible only after 24 h of hydration. However, GGBS dissolution was observed between 6-11h of hydration (and suspected before 6 h in the $CaCl_2$-accelerated sample), and showed to contribute to the microstructure development of slag-based blended cements at early ages.

Author contributions

S.B., L.S. and C.P. prepared the samples and performed the XMT analyses under the supervision of A.B. and M.O. A.B. developed the experimental setup. M.O. performed the beamline calibration and data pre-processing. M.P. post-processed the whole dataset and wrote the first draft of the article. C.N. provided the computational equipment, managed data post-processing, and initiated the image subtraction method. M.P., S.B., M.C. and C.P. participated in numerous meetings to discuss the results and all co-authors participated in reviewing and editing the article. M.C. and J.K. led the overall project and acquired funding.

Declaration of interests

The authors declare that they have no known competing financial interests or personal relationships that could have influenced the work reported in this paper.

Funding

This work was supported by ArcelorMittal Maizieres Research and the European Commission through the Research Fund for Coal and Steel (grant no 749809, 2017) on behalf of the Actislag project.

References

[1] H.F.W. Taylor, Cement chemistry, 2. ed., repr, Telford Publ, London, 2003.

[2] P.C. Hewlett, M. Liska, Lea's chemistry of cement and concrete, 5th edition, Oxford: Butterworth-Heinemann, 2019.

[3] B. Lothenbach, K. Scrivener, R.D. Hooton, Supplementary cementitious materials, Cem. Concr. Res. 41 (2011) 1244–1256. https://doi.org/10.1016/j.cemconres.2010.12.001.

[4] N. De Belie, M. Soutsos, E. Gruyaert, eds., Properties of Fresh and Hardened Concrete Containing Supplementary Cementitious Materials: State-of-the-Art Report of the RILEM Technical Committee 238-SCM, Working Group 4, Springer International Publishing, Cham, 2018. https://doi.org/10.1007/978-3-319-70606-1.

[5] J. Skibsted, R. Snellings, Reactivity of supplementary cementitious materials (SCMs) in cement blends, Cem. Concr. Res. 124 (2019) 105799. https://doi.org/10.1016/j.cemconres.2019.105799.

[6] S. Ramanathan, M. Croly, P. Suraneni, Comparison of the effects that supplementary cementitious materials replacement levels have on cementitious paste properties, Cem. Concr. Compos. 112 (2020) 103678. https://doi.org/10.1016/j.cemconcomp.2020.103678.

[7] G. Van Rompaey, Etude de la réactivité des ciments riches en laitier, à basse température et à temps court, sans ajout chloruré, Université libre de Bruxelles, 2006.

[8] V.S. Ramachandran, 5 - Accelerators, in: Concr. Admix. Handb. Second Ed., Park Ridge, NJ: William Andrew Publishing, 1996: pp. 185–285.

[9] K. Riding, D.A. Silva, K. Scrivener, Early age strength enhancement of blended cement systems by CaCl2 and diethanol-isopropanolamine, Cem. Concr. Res. 40 (2010) 935–946. https://doi.org/10.1016/j.cemconres.2010.01.008.

[10] F. Bellmann, J. Stark, Activation of blast furnace slag by a new method, Cem. Concr. Res. 39 (2009) 644–650. https://doi.org/10.1016/j.cemconres.2009.05.012.

[11] K. Scrivener, R. Snellings, B. Lothenbach, eds., A Practical Guide to Microstructural Analysis of Cementitious Materials, CRC Press, 2018. https://doi.org/10.1201/b19074.

[12] M. Parisatto, M.C. Dalconi, L. Valentini, G. Artioli, A. Rack, R. Tucoulou, G. Cruciani, G. Ferrari, Examining microstructural evolution of Portland cements by in-situ synchrotron micro-tomography, J. Mater. Sci. 50 (2015) 1805–1817. https://doi.org/10.1007/s10853-014-8743-9.

[13] J. Zhang, G.W. Scherer, Comparison of methods for arresting hydration of cement, Cem. Concr. Res. 41 (2011) 1024–1036. https://doi.org/10.1016/j.cemconres.2011.06.003.

[14] E. Gallucci, K. Scrivener, A. Groso, M. Stampanoni, G. Margaritondo, 3D experimental investigation of the microstructure of cement pastes using synchrotron X-ray microtomography (μCT), Cem. Concr. Res. 37 (2007) 360–368. https://doi.org/10.1016/j.cemconres.2006.10.012.

[15] W. Kong, Y. Wei, S. Wang, J. Chen, Y. Wang, Research progress on cement-based materials by X-ray computed tomography, Int. J. Pavement Res. Technol. 13 (2020) 366–375. https://doi.org/10.1007/s42947-020-0119-8.

[16] Z. Wu, Y. Wei, S. Wang, J. Chen, Application of X-Ray Micro-CT for Quantifying Degree of Hydration of Slag-Blended Cement Paste, J. Mater. Civ. Eng. 32 (2020) 04020008. https://doi.org/10.1061/(ASCE)MT.1943-5533.0003082.

[17] N. Burlion, D. Bernard, D. Chen, X-ray microtomography: Application to microstructure analysis of a cementitious material during leaching process, Cem. Concr. Res. 36 (2006) 346–357. https://doi.org/10.1016/j.cemconres.2005.04.008.

[18] S. Brisard, M. Serdar, P.J.M. Monteiro, Multiscale X-ray tomography of cementitious materials: A review, Cem. Concr. Res. 128 (2020) 105824. https://doi.org/10.1016/j.cemconres.2019.105824.

[19] C. Noiriel, B. Madé, P. Gouze, Impact of coating development on the hydraulic and transport properties in argillaceous limestone fracture, Water Resour. Res. 43 (2007). https://doi.org/10.1029/2006WR005379.

[20] C. Noiriel, L. Luquot, B. Madé, L. Raimbault, P. Gouze, J. van der Lee, Changes in reactive surface area during limestone dissolution: An experimental and modelling study, Chem. Geol. 265 (2009) 160–170. https://doi.org/10.1016/j.chemgeo.2009.01.032.

[21] C. Noiriel, Resolving time-dependent evolution of pore-scale structure, permeability and reactivity using X-ray microtomography, Rev. Mineral. Geochem. 80 (2015) 247–285. https://doi.org/10.2138/rmg.2015.80.08.
[22] D. Gastaldi, F. Canonico, L. Capelli, E. Boccaleri, M. Milanesio, L. Palin, G. Croce, F. Marone, K. Mader, M. Stampanoni, In situ tomographic investigation on the early hydration behaviors of cementing systems, Constr. Build. Mater. 29 (2012) 284–290. https://doi.org/10.1016/j.conbuildmat.2011.10.016.
[23] T.J. Chotard, M.P. Boncoeur-Martel, A. Smith, J.P. Dupuy, C. Gault, Application of X-ray computed tomography to characterise the early hydration of calcium aluminate cement, Cem. Concr. Compos. 25 (2003) 145–152. https://doi.org/10.1016/S0958-9465(01)00063-4.
[24] L. Helfen, F. Dehn, P. Mikulík, T. Baumbach, Three-dimensional imaging of cement microstructure evolution during hydration, Adv. Cem. Res. 17 (2005) 103–111. https://doi.org/10.1680/adcr.2005.17.3.103.
[25] K. Ji-Su, C. Sang-Yeop, S. Dietmar, H. Tong-Seok, Issues on characterization of cement paste microstructures from μ -CT and virtual experiment framework for evaluating mechanical properties, Constr. Build. Mater. 202 (2019) 82–102. https://doi.org/10.1016/j.conbuildmat.2019.01.030.
[26] A. Cuesta, Á.G. De la Torre, I. Santacruz, A. Diaz, P. Trtik, M. Holler, B. Lothenbach, M.A.G. Aranda, Quantitative disentanglement of nanocrystalline phases in cement pastes by synchrotron ptychographic X-ray tomography, IUCrJ. 6 (2019) 473–491. https://doi.org/10.1107/S2052252519003774.
[27] T. Deboodt, J.H. Ideker, O.B. Isgor, D. Wildenschild, Quantification of synthesized hydration products using synchrotron microtomography and spectral analysis, Constr. Build. Mater. 157 (2017) 476–488. https://doi.org/10.1016/j.conbuildmat.2017.09.031.
[28] M. Zhang, Y. He, G. Ye, D.A. Lange, K. van Breugel, Computational investigation on mass diffusivity in Portland cement paste based on X-ray computed microtomography (μCT) image, Constr. Build. Mater. 27 (2012) 472–481. https://doi.org/10.1016/j.conbuildmat.2011.07.017.
[29] L. Steger, S. Blotevogel, L. Frouin, C. Patapy, M. Cyr, Experimental evidence for the acceleration of slag hydration in blended cements by the addition of CaCl2, Cem. Concr. Res. (n.d.) accepted for publication.
[30] D. Paganin, S.C. Mayo, T.E. Gureyev, P.R. Miller, S.W. Wilkins, Simultaneous phase and amplitude extraction from a single defocused image of a homogeneous object, J. Microsc. 206 (2002) 33–40. https://doi.org/10.1046/j.1365-2818.2002.01010.x.
[31] F. Marone, M. Stampanoni, Regridding reconstruction algorithm for real-time tomographic imaging, J. Synchrotron Radiat. 19 (2012) 1029–1037. https://doi.org/10.1107/S0909049512032864.
[32] K. Olivier, A. Darquennes, F. Benboudjema, R. Gagné, Early-Age Self-Healing of Cementitious Materials Containing Ground Granulated Blast-Furnace Slag under Water Curing, J. Adv. Concr. Technol. 14 (2016) 717–727. https://doi.org/10.3151/jact.14.717.
[33] Y.-L. Li, X.-L. Zhao, R.K. Singh Raman, S. Al-Saadi, Thermal and mechanical properties of alkali-activated slag paste, mortar and concrete utilising seawater and sea sand, Constr. Build. Mater. 159 (2018) 704–724. https://doi.org/10.1016/j.conbuildmat.2017.10.104.
[34] W.-J. Long, B.-X. Xiao, Y.-C. Gu, F. Xing, Micro- and macro-scale characterization of nano-SiO2 reinforced alkali activated slag composites, Mater. Charact. 136 (2018) 111–121. https://doi.org/10.1016/j.matchar.2017.12.013.
[35] X. Zhu, Z. Zhang, K. Yang, B. Magee, Y. Wang, L. Yu, S. Nanukuttan, Q. Li, S. Mu, C. Yang, M. Basheer, Characterisation of pore structure development of alkali-activated slag cement during early hydration using electrical responses, Cem. Concr. Compos. 89 (2018) 139–149. https://doi.org/10.1016/j.cemconcomp.2018.02.016.
[36] B. Šavija, H. Zhang, E. Schlangen, Micromechanical testing and modelling of blast furnace slag cement pastes, Constr. Build. Mater. 239 (2020) 117841. https://doi.org/10.1016/j.conbuildmat.2019.117841.
[37] F. Han, J. Liu, P. Yan, Comparative study of reaction degree of mineral admixture by selective dissolution and image analysis, Constr. Build. Mater. 114 (2016) 946–955. https://doi.org/10.1016/j.conbuildmat.2016.03.221.

[38] B. Li, Q. Li, W. Chen, Spatial zonation of a hydrotalcite-like phase in the inner product of slag: New insights into the hydration mechanism, Cem. Concr. Res. 145 (2021) 106460. https://doi.org/10.1016/j.cemconres.2021.106460.
[39] A. Rodríguez, S. Gutiérrez-González, M.I. Prieto, A. Cobo, V. Calderón, Analysis of long-term corrosion behavior in mortars containing recycled ladle furnace slag using computerized tomography and SEM: Long-term corrosion behavior in mortars with slag, Mater. Corros. 66 (2015) 199–205. https://doi.org/10.1002/maco.201407697.
[40] K. Wan, Q. Xu, Local porosity distribution of cement paste characterized by X-ray micro-tomography, Sci. China Technol. Sci. 57 (2014) 953–961. https://doi.org/10.1007/s11431-014-5513-5.
[41] M. Fan, Y. Chen, K. Wan, Representative elementary volume analysis of hardened cement paste during hydration using X-ray Computed Tomography, Constr. Build. Mater. 277 (2021) 122268. https://doi.org/10.1016/j.conbuildmat.2021.122268.
[42] A.C. Olivieri, N.M. Faber, Validation and error, in: Compr. Chemom. Chem. Biochem. Data Anal., Elsevier, 2009: pp. 91–120. https://doi.org/10.1016/B978-044452701-1.00073-9.
[43] F. Bernachy-Barbe, T. Sayari, V. Dewynter-Marty, V. L'Hostis, Using X-ray microtomography to study the initiation of chloride-induced reinforcement corrosion in cracked concrete, Constr. Build. Mater. 259 (2020) 119574. https://doi.org/10.1016/j.conbuildmat.2020.119574.
[44] Y. Tanabe, T. Kido, A. Kurata, T. Kouchi, N. Fukuyama, T. Yokoi, T. Uetani, N. Yamashita, M. Miyagawa, T. Mochizuki, Late iodine enhancement computed tomography with image subtraction for assessment of myocardial infarction, Eur. Radiol. 28 (2018) 1285–1292. https://doi.org/10.1007/s00330-017-5048-9.
[45] D. Grob, L.J. Oostveen, M. Prokop, C.M. Schaefer-Prokop, I. Sechopoulos, M. Brink, Imaging of pulmonary perfusion using subtraction CT angiography is feasible in clinical practice, Eur. Radiol. 29 (2019) 1408–1414. https://doi.org/10.1007/s00330-018-5740-4.
[46] J.D. Lawson, E. Schreibmann, A.B. Jani, T. Fox, Quantitative evaluation of a cone-beam computed tomography-planning computed tomography deformable image registration method for adaptive radiation therapy, J. Appl. Clin. Med. Phys. 8 (2007) 96–113. https://doi.org/10.1120/jacmp.v8i4.2432.
[47] M.C.G. Juenger, P.J.M. Monteiro, E.M. Gartner, G.P. Denbeaux, A soft X-ray microscope investigation into the effects of calcium chloride on tricalcium silicate hydration, Cem. Concr. Res. 35 (2005) 19–25. https://doi.org/10.1016/j.cemconres.2004.05.016.
[48] K. Essam A., A. Doaa A., M. Maha R., N. Rehab, Effect of calcium chloride on the hydration characteristics of ground clay bricks cement pastes, Beni-Suef Univ. J. Basic Appl. Sci. 2 (2013) 20–30. https://doi.org/10.1016/j.bjbas.2013.09.003.
[49] T. Vehmas, A. Kronlöf, A. Cwirzen, Calcium chloride acceleration in ordinary Portland cement, Mag. Concr. Res. 70 (2018) 856–863. https://doi.org/10.1680/jmacr.17.00079.
[50] L. Steger, Etude de l'accélération des ciments à haute teneur en laitier de haut-fourneaux par du chlorure de calcium, Université Paul Sabatier Toulouse III, 2019.